Enhancing the multi-tone continuous-wave lidar with phase detection

Bayer, M. Mert, Guentchev, George, Li, Xun, Velazco, Jose, Boyraz, Ozdal

M. Mert Bayer, George N. Guentchev, Xun Li, Jose E. Velazco, Ozdal Boyraz, "Enhancing the multi-tone continuous-wave lidar with phase detection," Proc. SPIE 11828, ODS 2021: Industrial Optical Devices and Systems, 1182807 (7 September 2021); doi: 10.1117/12.2596162

SPIE.

Event: SPIE Optical Engineering + Applications, 2021, San Diego, California, United States

Enhancing the multi-tone continuous-wave lidar with phase detection

M. Mert Bayer*[a], George N. Guentchev [a], Xun Li [a], Jose E. Velazco [b], Ozdal Boyraz [a]
[a]Electrical Engineering and Computer Science Department, University of California, Irvine, CA 92697, USA; [b] Jet Propulsion Laboratory, Pasadena, CA 91109, USA

ABSTRACT

Over the past years, light detection and ranging (lidar) technologies have been investigated and commercialized for various applications such as autonomous vehicles, terrestrial mappings, and precision measurements. Currently, the frequently used ranging methods are the pulsed time of flight (PToF) and frequency modulated continuous wave (FMCW) lidars that relies on frequency sweeping to capture range and velocity information. We have previously developed and demonstrated the multi-tone continuous wave (MTCW) that operates by employing amplitude modulation via multiple radio frequencies (RF) and coherent detection. Here, we present a theoretical and experimental study on phase-based MTCW lidar that can detect the range and velocity of objects with arbitrary velocities. The experiments demonstrate that the phase and frequency of the Doppler-shifted fixed RF tones can be used to extract the range and velocity information in a single shot measurement. We show that a <±1cm resolution in the ranging, limited by the temporal resolution of the detection system, and a 0.5cm/s speed resolution is limited by the frequency resolution of the detection system are achievable. Moreover, the proposed approach has the potential to mitigate the requirement for a narrow linewidth laser for coherent detection.

Keywords: Lidar, Continuous-Wave Lidar, Photonic Doppler Velocimetry, Coherent Ranging

1. INTRODUCTION

The light detection and ranging (lidar) market is rapidly expanding due to the vast demand for various applications such as self-driving cars, airborne altimetry, precision measurements, and robotics[1–4]. Nowadays, lidars are built by using two different optical backbones, namely time-of-flight (ToF) or coherent detection[5,6]. The ToF lidars rely on the time information encoded in the propagation of a high peak power laser pulse. The echo signal returns to the detector with a certain delay of Δt compared to the master clock; hence the target distance (L) can be estimated as $L = c \times \Delta t / 2$ with respect to the speed of light (c)[7]. The necessity of short pulse generation and high temporal resolution limits the ToF lidars by requiring fast electronics[8]. Moreover, the ToF lidars are inherently handicapped to perform simultaneous velocimetry. To acquire the target speed as well as the distance, the ToF architecture utilizes multiple frames of the target to compute the speed (v) as $v = dx / dt$, where dx and dt represent the change in position and time between frames, respectively.

The second school of lidars utilizes coherent detection by employing continuous wave (CW) lasers. The general principle of the CW-based lidars is realized through the beating of the echo signal with a local oscillator, which is generally a fraction of the light before leaving the lidar architecture[9]. There are various kinds of CW lidars such as amplitude-modulated (AMCW), frequency-modulated (FMCW), phase-based, and modulation-based lidars[10–12]. Among all, FMCW is currently the most trendy and attention-grabbing coherent ranging technique. In this method, the frequency of a narrow linewidth CW laser is modulated, and a chirp is realized on the signal. The modulated light is split into two to realize the local oscillator before leaving the transmission collimator. The phase-delayed echo signal beats with the local oscillator to generate a beat note as $f_{beat} = \Delta t \times 2B / T$, where B and T are bandwidth and frequency sweep period, respectively. Thus, it is possible to acquire the target location. FMCW lidars can perform simultaneous velocimetry by exploiting the Doppler effect. Compared to the ToF alternatives, FMCW lidars have better detection sensitivity and the ability to perform velocimetry[13]. However, FMCW lidars require chirp linearization and narrow linewidth laser sources that make the implementation of the coherent lidars very challenging[14,15].

As an alternative to the coherent lidars, previously, we introduced the Multi-Tone Continuous-Wave (MTCW) lidar that employs multiple radio-frequency (RF) modulations on a CW laser[16,17]. The individual sidebands realize different amounts of phase shifts during their propagation. A portion of the modulated light is also kept as a local oscillator to realize interference with the echo signal. The interference of both lights yields variations over the amplitudes of the sidebands that

ODS 2021: Industrial Optical Devices and Systems, edited by Ryuichi Katayama, Yuzuru Takashima, Proc. of SPIE Vol. 11828, 1182807 · © 2021 SPIE
CCC code: 0277-786X/21/$21 · doi: 10.1117/12.2596162

can be used to compute the target distance. We have already demonstrated stationary and dynamic-target ranging with the amplitude-based MTCW lidar[18–20]. We also showed a technique to improve the ranging via MTCW lidar for fast dynamic targets by utilizing the actual tone phases[21]. In this work, we present the phase-based MTCW lidar (PB-MTCW) that provides a solution to both chirp linearization and narrow linewidth laser requirements of FMCW lidars. The renewed configuration along with the range triangulation algorithm enables the PB-MTCW lidar to perform ranging without employing any form of phase, frequency, or amplitude sweep by solely comparing the individual tone phases that enable coherent ranging beyond the coherence length of the laser.

2. THEORETICAL MODELLING OF THE PB-MTCW LIDAR

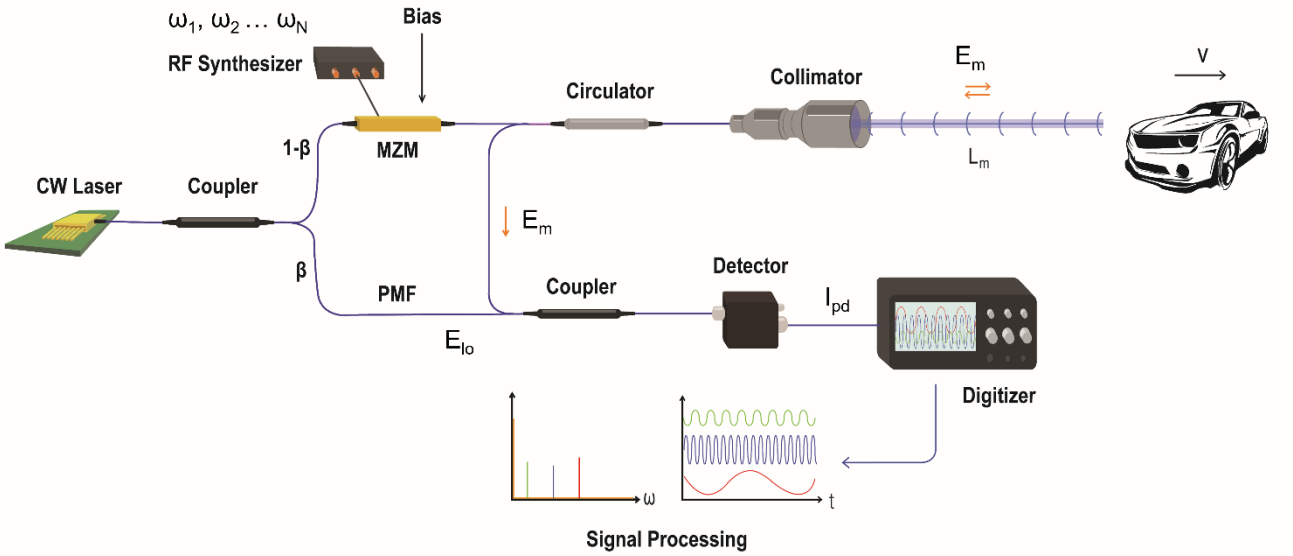

Figure 1. Schematic of the proposed PB-MTCW lidar.

The proposed schematic of the PB-MTCW lidar is shown in Figure 1. Here, a CW laser is split into two with a coupling factor of β. One arm is kept as a local oscillator through polarization-maintaining fibers (PMF) to prevent any polarization issues. The electric field (E-field) of the local oscillator can be formalized as $E_{lo} = A_0 \alpha_f \sqrt{\beta} \exp(j\omega_0 t + j\phi_0 + j\phi_n(t))$ where $A_0 = \sqrt{P_{out}}$ is the amplitude, ω_0 is the angular frequency, ϕ_0 is the initial phase of the source laser, α_f is the attenuation inside the fiber and $\phi_n(t)$ represents the laser phase noise at the local oscillator branch. Moreover, the second branch after the coupler is modulated via a Mach-Zehnder modulator (MZM) with push-pull configuration under quadrature bias by RF synthesizers. A total of N RF tones are fed to the MZM with the following E-field $E_{RF} = \sum_{i=1}^{N} A_i^{RF} \cos\left(\omega_i t + \phi_i^{RF}\right)$, where ω_i is the modulation tone frequency and ϕ_i^{RF} is the initial phase of the i^{th} RF tone. The light inside the fiber is carried to free space through a collimator and a circulator is used to separate the transmission and reception signals. Each modulation tone and the optical carrier frequency realize a phase shift proportional to the target distance. The time delay due to propagation can be formalized as $\tau = 2L_m / c$, where L_m is the range of target-under-test (TUT) and c is the speed of light. The expected E-field equation of the echo signal is given in Eq.(1) for a stationary target. Here, m is the modulation depth and α_m is the linear attenuation coefficient representing the potential scattering losses in the measurement path.

$$
\begin{aligned}
E_m = {} & \frac{A_0}{2\sqrt{2}} \alpha_m \alpha_f \sqrt{1-\beta} \exp\left[j\omega_0 t + j\phi_0 + j\omega_0 \tau + j\phi_n(t-\tau) \right] \\
& - \frac{mA_0}{4\sqrt{2}} \alpha_m \alpha_f \sqrt{1-\beta} \sum_{i=1}^{N} \left(\begin{array}{l} \exp\left[j(\omega_0 + \omega_i)t + j\phi_0 + j\phi_i^{RF} + j(\omega_0 + \omega_i)\tau + j\phi_n(t-\tau) \right] \\ + \exp\left[j(\omega_0 - \omega_i)t + j\phi_0 - j\phi_i^{RF} + j(\omega_0 - \omega_i)\tau - j\phi_n(t-\tau) \right] \end{array} \right)
\end{aligned}
\tag{1}
$$

The collected light is combined with the local oscillator via a coupler and the square-law detector with a responsivity R, yields the photocurrent as $I_{pd} = R\left(E_m + E_{lo}\right)\cdot\left(E_m + E_{lo}\right)^*$. The I_{pd} equation of a stationary target is shown in Eq.(2), where the laser phase noise difference of E_m and E_{lo} is represented as $\Phi(t,\tau) = \phi_n(t) - \phi_n(t-\tau)$.

$$
\begin{aligned}
I_{pd} &= RA_0^2\alpha_f^2\beta + \frac{3RA_0^2\alpha_m^2\alpha_f^2(1-\beta)}{16} + \frac{RA_0^2\alpha_m\alpha_f^2\sqrt{\beta}\sqrt{1-\beta}}{\sqrt{2}}\cos\left(\omega_0\tau + \Phi(t,\tau)\right) \\
&- \frac{RmA_0^2\alpha_m\alpha_f^2\sqrt{\beta}\sqrt{1-\beta}}{2\sqrt{2}}\left[\begin{array}{l}\sum_{i=1}^{N}\cos\left(\omega_i t + (\omega_0+\omega_i)\tau + \phi_i^{RF} + \Phi(t,\tau)\right) \\ +\sum_{i=1}^{N}\cos\left(\omega_i t - (\omega_0-\omega_i)\tau - \phi_i^{RF} - \Phi(t,\tau)\right)\end{array}\right] \\
&+ \frac{RmA_0^2\alpha_m^2\alpha_f^2(1-\beta)}{8}\left[\sum_{i=1}^{N}\cos\left(\omega_i t + \omega_i\tau + \phi_i^{RF}\right) + \sum_{i=1}^{N}\cos\left(\omega_i t + \omega_i\tau - \phi_i^{RF}\right)\right] \\
&+ \frac{Rm^2A_0^2\alpha_m^2\alpha_f^2(1-\beta)}{8}\sum_{i=1}^{N}\cos\left(2\omega_i t + 2\omega_i\tau\right)
\end{aligned}
\tag{2}
$$

In the case of a dynamic target with a velocity v, the echo signal will realize a Doppler frequency shift based on the target speed as $\omega_d = (2v/c)\omega_0$. Similarly, each modulation frequency will realize a Doppler shift ω_d^i, as well. The echo signal E-field of a dynamic TUT is shown in Eq.(3).

$$
\begin{aligned}
E_m &= \frac{A_0}{2\sqrt{2}}\alpha_m\alpha_f\sqrt{1-\beta}\exp\left(j(\omega_0+\omega_d)t + j\omega_0\frac{\tau}{2} + j(\omega_0+\omega_d)\frac{\tau}{2} + j\phi_0 + j\phi_n(t-\tau)\right) \\
&- \frac{mA_0}{4\sqrt{2}}\alpha_m\alpha_f\sqrt{1-\beta}\sum_{i=1}^{N}\left(\begin{array}{l}\exp\left[\begin{array}{l}j(\omega_0+\omega_i+\omega_d+\omega_d^i)t + j(\omega_0+\omega_i)\frac{\tau}{2} \\ +j(\omega_0+\omega_i+\omega_d+\omega_d^i)\frac{\tau}{2} + j(\phi_0+\phi_i^{RF}) + j\phi_n(t-\tau)\end{array}\right] \\ +\exp\left[\begin{array}{l}j(\omega_0-\omega_i+\omega_d-\omega_d^i)t + j(\omega_0-\omega_i)\frac{\tau}{2} \\ +j(\omega_0-\omega_i+\omega_d-\omega_d^i)\frac{\tau}{2} + j(\phi_0-\phi_i^{RF}) + j\phi_n(t-\tau)\end{array}\right]\end{array}\right)
\end{aligned}
\tag{3}
$$

The forward propagating and echoed light acquire different phases during their propagation due to the induced Doppler frequency shift. It is possible to assume $\omega_d + \omega_d^i \simeq \omega_d - \omega_d^i \simeq \omega_d$ by comparing $\omega_0 >> \omega_i$. Unless the target is moving at extreme velocities, this assumption is always true for most practical applications. Therefore, the resultant I_{pd} of a moving target is given in Eq.(4).

$$
\begin{aligned}
I_{pd} &= R\beta A_0^2\alpha_f^2 + \frac{R(1-\beta)A_0^2\alpha_m^2\alpha_f^2}{8} + \frac{Rm(1-\beta)A_0^2\alpha_m^2\alpha_f^2}{16} \\
&+ \frac{Rm\sqrt{\beta}\sqrt{(1-\beta)}A_0^2\alpha_m\alpha_f^2}{\sqrt{2}}\cos\left(\omega_d t + \omega_o\tau + \omega_d\frac{\tau}{2} + \Phi(t,\tau)\right) \\
&- \frac{Rm(1-\beta)A_0^2\alpha_m^2\alpha_f^2}{8}\sum_{i=1}^{N}\cos\left(\omega_i t + \omega_i\tau + \phi_i^{RF}\right) + \frac{Rm(1-\beta)A_0^2\alpha_m^2\alpha_f^2}{16}\sum_{i=1}^{N}\cos\left(2\omega_i t + 2\omega_i\tau\right) \\
&- \frac{Rm\sqrt{\beta}\sqrt{(1-\beta)}A_0^2\alpha_m\alpha_f^2}{2\sqrt{2}}\sum_{i=1}^{N}\cos\left((\omega_i+\omega_d)t + (\omega_o+\omega_i)\tau + \omega_d\frac{\tau}{2} + \phi_i^{RF} + \Phi(t,\tau)\right) \\
&- \frac{Rm\sqrt{\beta}\sqrt{(1-\beta)}A_0^2\alpha_m\alpha_f^2}{2\sqrt{2}}\sum_{i=1}^{N}\cos\left((\omega_i-\omega_d)t - (\omega_o-\omega_i)\tau - \omega_d\frac{\tau}{2} - \phi_i^{RF} - \Phi(t,\tau)\right)
\end{aligned}
\tag{4}
$$

3. POST-PROCESSING

After acquiring the phase-shifted RF modulation tones via photodetector, it is possible to extract the range and velocity information by comparing individual tone phases and frequencies. In particular, by considering the impact of potential scattering losses in Eq.(2), the equation of the tones can be simplified as $2A_i \cos\left(\omega_0\tau + \phi_i^{RF} + \Phi(t,\tau)\right)\cos(\omega_i t + \omega_i \tau)$, where A_i is the tone amplitude, the first cosine term depicts the amplitude, and the second cosine term indicates the frequency and phase of the detected RF modulation. Similarly, for a dynamic TUT, a single tone can be defined by analyzing the $\omega_i \pm \omega_d$ sidebands and the definition is $A_i \cos\left((\omega_i \pm \omega_d)t \pm (\omega_o \pm \omega_i)\tau \pm \omega_d \frac{\tau}{2} \pm \phi_i^{RF} \pm \Phi(t,\tau)\right)$. To generate the distance of the TUT, we mix the individual RF tones at ω_i and ω_j ($i \neq j$). The result of the digital or electronic mixing yields intermediate frequencies (IF) as $A_i A_j \cos\left(\Delta\omega_{i,j} t \pm \Delta\phi_{i,j}\right)$, where $\Delta\phi_{i,j}$, and $\Delta\omega_{i,j}$ corresponds to the phase and frequency difference of i^{th} and j^{th} tones, respectively. This inter-tonal process allows eliminating the common phase and frequency terms related to the optical carrier and Doppler shift, thus the noise-free IF tones can manifest the range of the TUT as $L_m = \left(2\pi n + \Delta\phi_{i,j}\right)c / \Delta\omega_{i,j}$, where n is an integer pointing out the 2π-modulo cyclic behavior of the phase.

		l		
		$\omega_3 - \omega_2$	$\omega_3 - \omega_1$	$\omega_2 - \omega_1$
	1	$k = 1$	$k = 1$	$k = 1$
	2	$k = 2$	repeat	repeat
	3	$k = 3$	repeat	repeat
	4	$k = 4$	repeat	repeat
	⋮	⋮	repeat	k = 2-10
	300	$k = 300$	$k = 2$	$k = 11$
k	**301**	$k = 301$	repeat	repeat
	302	$k = 302$	repeat	repeat
	⋮	⋮	$k = 3$	k = 12-17
	498	$k = 498$	repeat	$k = 18$
	499	$k = 499$	repeat	repeat
	500	$k = 500$	repeat	repeat

Figure 2. Illustration of data matrix $M_{k,l}$ for a 3-tone PB-MTCW lidar with ω_1, ω_2, and ω_3. The k values in the matrix represent the value of n in $L_m = L_0^{i,j} + \left(2\pi nc / \Delta\omega_{i,j}\right)$. The repetitive terms, where the k values are equal in the consecutive rows are indicated in the matrix as repeat.

The utilization of multiple RF tones allows the PB-MTCW lidar to generate the TUT distance by triangulation. For a given $\Delta\phi_{i,j}$, only the initial range of the target can be found as $L_0^{i,j} = c\Delta\phi_{i,j} / \Delta\omega_{i,j}$. It is possible to acquire a total of $\binom{N}{2}$ possible $L_0^{i,j}$ for a stationary target, whereas the targets in motion will yield $\binom{2N}{2}$ results. Then the target distance can be computed as $L_m = L_0^{i,j} + \left(2\pi nc / \Delta\omega_{i,j}\right)$. There will be multiple solutions of L_m for each integer value of n. However, the resultant L_m should have a common solution for each $\Delta\omega_{i,j}$, which will be the actual target distance. To realize this, n is scanned, and all the resultant L_m are concatenated in a data matrix $M_{k,l}$, where k is equal to nmax and l is the number of available $\Delta\omega_{i,j}$. Here, we set the maximum anticipated range of a target by selecting the maximum value of n (n_{max}). In practice, this range is determined by the optical system loss or the application. The standard deviation of each row is computed as $\sigma_k = \sqrt{\sum_{r=1}^{l}\left(M_{k,r} - \overline{M}_k\right)^2 / l}$, where $\overline{M}_k$ is the mean value of the k^{th} row. The $\overline{M}_k$ of the row that

yields the minimum standard deviation corresponds to the actual measurement distance. For illustration, a sample $M_{k,l}$ matrix is presented in Figure 2 for a 3-tone system with n_{max} assumed to be 500, and the repetitive terms are indicated in the matrix. The computed standard deviation will follow a certain pattern based on the sweeping limits. The minimum σ_k will repeat itself in an interval of 0cm to $L_{rep} = 2\pi c / \omega_{\text{gcd}}$, where ω_{gcd} stands for the frequency equal to the greatest common divisor of the used $\Delta\omega_{i,j}$ in the algorithm. The selection of the RF tones in a fashion to maximize the L_{rep} will improve the maximum measurement range. Moreover, the introduction of a quasi-CW pulsation through an additional optical modulator to the measurement branch will facilitate higher signal-to-noise ratio measurements, as well as potential time gating to generate coarse range information to limit the scanning of n. Hence, it can alleviate the repetitive behavior of the minimum standard deviation point to acquire L_m through the triangulation algorithm.

4. METHODOLOGY

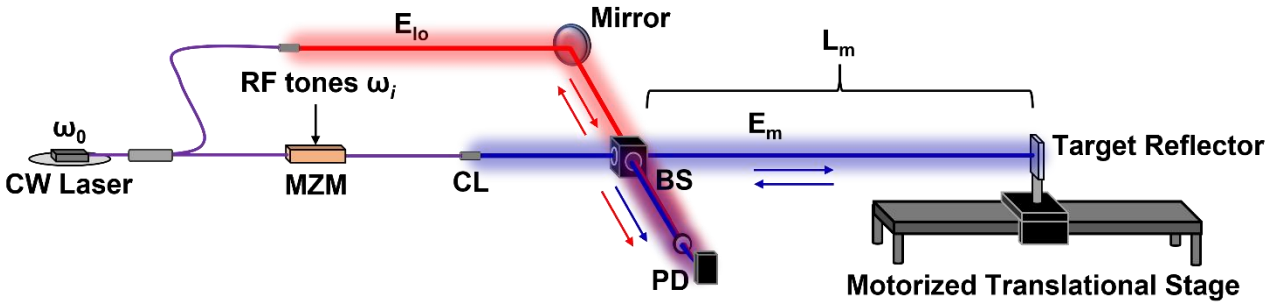

Figure 3. The PB-MTCW experimental setup. Mach-Zehnder Modulator (MZM), collimator (CL), beamsplitter (BS), and photodetector (PD).

Figure 3 illustrates the experimental setup to perform ranging and velocimetry of static and dynamic targets. Here, we modulate a <100kHz linewidth 1064nm CW laser with an MZM. The four modulation frequencies are 500, 700, 850, and 950MHz. The tones are carefully selected to prevent the cross-beating or second harmonic overlaps in between the tones. Tones are generated through phase-locked RF synthesizers and triggered by a common clock that also triggers the oscilloscope. The greatest common divisor of the selected tones is 50MHz that results in ~3m L_{rep} of the minimum standard deviation to obtain the target distance. Thus, the target is placed ~102cm away from the output facet of the beamsplitter (BS) for static target ranging. After being combined in a 4-way RF power splitter, the tones are transmitted to the MZM, which is biased around the quadrature voltage. The modulated light is delivered to free space by a collimator to perform the ranging and velocimetry. Furthermore, an additional collimator is utilized to establish the local oscillator in free space. The two collimators are stationed in a manner to crisscross the light beams from two branches. A 50/50 BS is positioned at the intersection point of two beams. The free space light detection is accomplished by a high-speed PIN photodetector and the coupling is optimized via a microscope lens. A target reflector is carried by a motorized translational stage and aligned away from the output facet of the BS. In addition, to acquire the initial tone-phases due to the RF synthesizers and the fiber path, a calibration mirror is placed closed to the BS. The post-processing algorithm first generates a pseudo measurement distance at the calibration mirror that is set as the zero-point for the lidar system before performing actual measurements of the TUT.

After the acquisition, measurement data is interpolated to 2^{23} data points to improve the resolution that significantly decreases potential distortions, since there is a high dependency of the phases on the time resolution during the data processing. The time-domain data is converted to the frequency domain using fast Fourier transform (FFT) to locate the sidebands and obtain the Doppler shifts for the dynamic target. A digital second-order bandpass Butterworth filter with a 1MHz bandwidth is used around each measured modulation tone. Zero-phase distortion filtering of the data is achieved by applying the filter in both forward and reverse directions to compensate for the phase of the filter[22]. Then the phases of the individual tones are acquired by comparing the filtered tones with their frequency-matched zero-phase digital cosine equivalents. Finally, the triangulation is performed by setting the scan length of the integer n to 20, which extends the scanning range of the lidar up to ~15m.

5. RESULTS AND DISCUSSION

The first experiment is performed by placing the target around 102cm away from the BS. The coarse distance of the target is measured via measurement tape for a sanity check before performing the ranging. The result of the triangulation algorithm is presented in Figure 4 as the black solid line and minimum standard deviation value is indicated with the red circle. The minimum σ corresponds to a target distance of 102.3cm. After 10 trials the standard deviation of all the measurements is <1cm indicating the ranging accuracy of the PB-MTCW methodology. This can also be attributed to the temporal resolution of the measurement by affecting the phase measurements as $\Delta L = c \times dt$, which is ~0.7cm in our measurement[21]. Moreover, to show the theoretical expectation, we performed a numerical simulation of the same system by setting the measurement distance to 102.3m. The final output of the triangulation algorithm by using the simulated I_{pd} is presented in Figure 4 by the blue dashed line. The minimum σ matches with the experimental results by yielding a σ very close to 0. In a noise-free or ideal environment, the expected minimum σ is 0, however, due to the small distortions over the RF tones caused by the synthesizers and detection electronics, the experimental minimum is found as 0.235. Increasing the number of modulation frequencies will improve the response of the triangulation algorithm by expanding the number of potential RF mixing combinations.

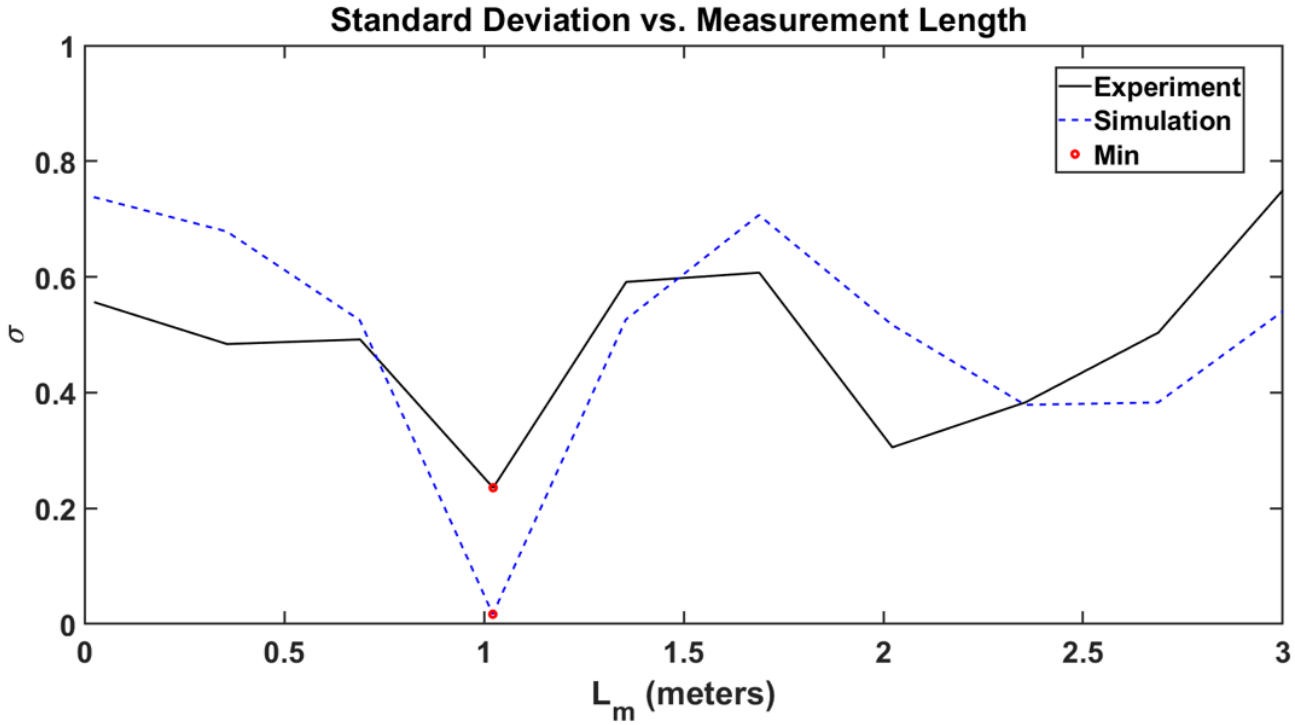

Figure 4. Experimental and simulation results of stationary target ranging for a target positioned at L_m=102cm.

We performed the second experiment by setting the translational stage to oscillate at a certain speed. The stage is set to operate at a speed <10cm/s, which is verified by the specs of the motor. The data is captured at the instant when the target is at the midsection of the stage that corresponds to ~103cm. It is not possible to conduct a sanity check by physical measurement methods due to the motion of the TUT. However, we limited the measurement range to ±5cm of the middle portion of the translational stage. The acquired I_{pd} spectrum is shown in Figure 5(a), where the modulation and Doppler-shifted frequencies are indicated. By utilizing the shifted frequencies at the baseband, it is possible to recover the velocity information of the target that is 8.65cm/s, which matches with the specs of the motorized stage. Also, the measured Doppler shift is 162.5kHz. The speed resolution of the PB-MTCW lidar depends on the frequency step size ($d\omega$) as $\Delta v = \left(\pm d\omega / \omega_0\right) c$. In our case, this is 0.53cm/s due to the 5kHz frequency resolution due to the measurement settings. Moreover, Figure 5(b) represents the result of the triangulation of the moving target by using the phases of $\omega_i \pm \omega_d$. The minimum σ is found at L_m=106.1cm, which is within the predetermined target range. Therefore, the PB-MTCW lidar is capable of performing single-shot ranging and velocimetry.

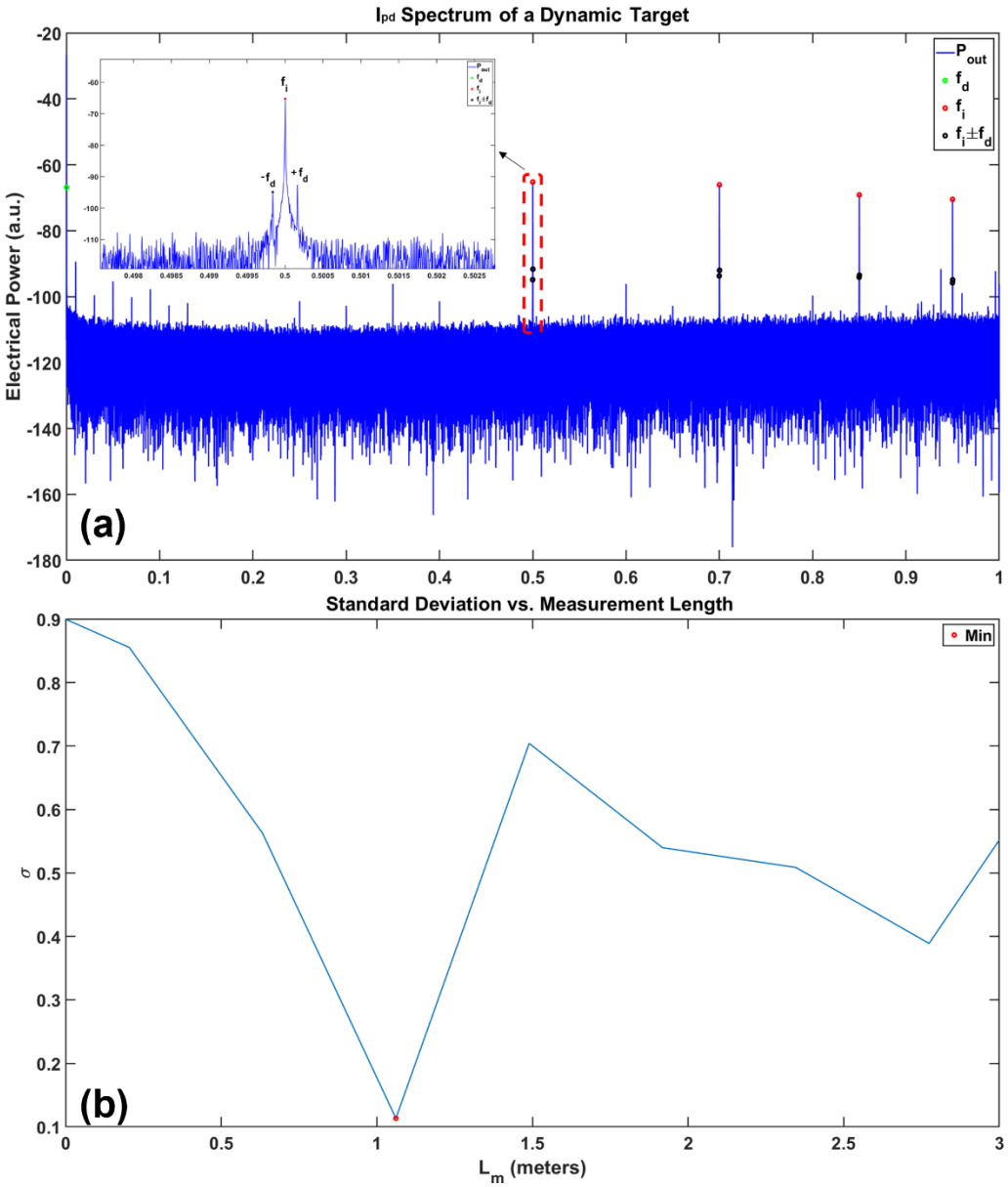

Figure 5. (a) Acquired I_{pd} spectrum of the dynamic target with 4 RF tones. Inset shows the magnified spectral region in the vicinity of 500MHz to show the $\pm f_d$, which are used to estimate the target speed. (b) Experimental result of the triangulation algorithm, where the minimum σ corresponds to L_m=106.1cm.

6. CONCLUSION

In this work, we demonstrate the theoretical background of the PB-MTCW lidar for single-shot static and dynamic target ranging and velocimetry. We explain the required post-processing and triangulation algorithms to realize ranging. Similarly, we show the Doppler shifts realized by the RF tones and the optical carrier can yield the target velocity. The experimental and simulation results for the stationary target ranging are presented, as well as the dynamic target ranging and velocimetry measurements. As a result, we demonstrate the capability of PB-MTCW lidar that provides solutions to two important limitations of FMCW lidar, which are the sweeping linearity and the coherence length of the CW laser. PB-MTCW uses multiple phase-locked individual RF tones that don't require any form of frequency or phase sweeping. In addition, the RF mixing of the acquired sidebands eliminates the common noise terms, which pave the way to overcome

the limitations of the laser phase noise. Therefore, PB-MTCW lidar can be a competitive alternative when integrated with quasi-CW pulsation for long-range remote sensing applications.

7. ACKNOWLEDGEMENTS

This work was supported by the Office of Naval Research under grant number # N00014-18-1-2845.

8. REFERENCES

[1] Urmson, C., Anhalt, J., Bagnell, D., Baker, C., Bittner, R., Clark, M., Dolan, J., Duggins, D., Galatali, T. and Geyer, C., "Autonomous driving in urban environments: Boss and the urban challenge," Journal of Field Robotics **25**(8), 425–466 (2008).

[2] Hecht, J., "Lidar for self-driving cars," Optics and Photonics News **29**(1), 26–33 (2018).

[3] Wallace, L., Lucieer, A., Watson, C. and Turner, D., "Development of a UAV-LiDAR system with application to forest inventory," 6, Remote Sensing **4**(6), 1519–1543 (2012).

[4] Bufton, J. L., Garvin, J. B., Cavanaugh, J. F., Ramos-Izquierdo, L. A., Clem, T. D. and Krabill, W. B., "Airborne lidar for profiling of surface topography," 1, Optical Engineering **30**(1), 72–79 (1991).

[5] Lee, J., Kim, Y.-J., Lee, K., Lee, S. and Kim, S.-W., "Time-of-flight measurement with femtosecond light pulses," 10, Nature Photonics **4**(10), 716 (2010).

[6] Jiang, Y., Karpf, S. and Jalali, B., "Time-stretch LiDAR as a spectrally scanned time-of-flight ranging camera," Nature Photonics **14**(1), 14–18 (2020).

[7] Behroozpour, B., Sandborn, P. A., Wu, M. C. and Boser, B. E., "Lidar system architectures and circuits," 10, IEEE Communications Magazine **55**(10), 135–142 (2017).

[8] Myllylä, R., Marszalec, J., Kostamovaara, J., Mäntyniemi, A. and Ulbrich, G.-J., "Imaging distance measurements using TOF lidar," Journal of Optics **29**(3), 188–193 (1998).

[9] Poulton, C. V., Yaacobi, A., Cole, D. B., Byrd, M. J., Raval, M., Vermeulen, D. and Watts, M. R., "Coherent solid-state LIDAR with silicon photonic optical phased arrays," 20, Optics Letters **42**(20), 4091–4094 (2017).

[10] Amann, M.-C., Bosch, T. M., Lescure, M., Myllylae, R. A. and Rioux, M., "Laser ranging: a critical review of unusual techniques for distance measurement," Optical Engineering **40** (2001).

[11] Peters, R. D., Lay, O. P., Dubovitsky, S., Burger, J. P. and Jeganathan, M., "MSTAR: an absolute metrology sensor with sub-micron accuracy for space-based applications" Proc. SPIE Vol. 10568, 105682O1-9 (2004).

[12] Rainey, K., Gilbertson, S., Kalb, D. and Beery, T., "Modulation based ranging for direct displacement measurements of a dynamic surface," Opt. Express **29**(14), 21174–21189 (2021).

[13] Riemensberger, J., Lukashchuk, A., Karpov, M., Weng, W., Lucas, E., Liu, J. and Kippenberg, T. J., "Massively parallel coherent laser ranging using a soliton microcomb," Nature **581**(7807), 164–170 (2020).

[14] Kim, T., Bhargava, P. and Stojanović, V., "Overcoming the Coherence Distance Barrier in Long-Range FMCW LIDAR," presented at CLEO: Science and Innovations, 2018, STh3L-7, Optical Society of America.

[15] Armstrong, J., "Theory of interferometric analysis of laser phase noise," JOSA **56**(8), 1024–1031 (1966).

[16] Torun, R., Bayer, M.M., Zaman, I.U. and Boyraz, O., "Multi-tone modulated continuous-wave lidar," Proc. SPIE 10925, 109250V1-9 (2019).

[17] Torun, R., Bayer, M.M., Zaman, I.U., Velazco, J. E. and Boyraz, O., "Realization of Multitone Continuous Wave Lidar," 4, IEEE Photonics Journal **11**(4), 1–10 (2019).

[18] Bayer, M. M., Torun, R., Li, X., Velazco, J. E. and Boyraz, O., "Simultaneous ranging and velocimetry with multi-tone continuous wave lidar," 12, Opt. Express **28**(12), 17241–17252 (2020).

[19] Bayer, M. M., Torun, R., Zaman, I. U. and Boyraz, O., "A Basic Approach for Speed Profiling of Alternating Targets with Photonic Doppler Velocimetry," Conference on Lasers and Electro-Optics, AW4K.4, Optical Society of America (2019).

[20] O. Boyraz, M. M. Bayer, R. Torun, and I. Zaman., "TuD2.2 - Multi Tone Continuous Wave Lidar (Invited)," IEEE Photonics Society Summer Topical Meeting Series (SUM), 1–2 (2019).

[21] Bayer, M. M. and Boyraz, O., "Ranging and velocimetry measurements by phase-based MTCW lidar," Opt. Express **29**(9), 13552–13562 (2021).

[22] Gustafsson, F., "Determining the initial states in forward-backward filtering," IEEE Transactions on signal processing **44**(4), 988–992 (1996).